

## BIPOLAR MAGNETIC SPOTS FROM DYNAMOS IN STRATIFIED SPHERICAL SHELL TURBULENCE

SARAH JABBARI<sup>1,2</sup>, AXEL BRANDENBURG<sup>1,2</sup>, NATHAN KLEEORIN<sup>3,1,4</sup>, DHRUBADITYA MITRA<sup>1</sup>, IGOR ROGACHEVSKII<sup>3,1,4</sup>

<sup>1</sup>Nordita, KTH Royal Institute of Technology and Stockholm University, Roslagstullsbacken 23, SE-10691 Stockholm, Sweden

<sup>2</sup>Department of Astronomy, AlbaNova University Center, Stockholm University, SE-10691 Stockholm, Sweden

<sup>3</sup>Department of Mechanical Engineering, Ben-Gurion University of the Negev, POB 653, Beer-Sheva 84105, Israel

<sup>4</sup>Department of Radio Physics, N. I. Lobachevsky State University of Nizhny Novgorod, Russia

*Draft version November 17, 2014*

### ABSTRACT

Recent work by Mitra et al. (2014) has shown that in strongly stratified forced two-layer turbulence with helicity and corresponding large-scale dynamo action in the lower layer, a magnetic field occurs in the upper layer in the form of sharply bounded bipolar magnetic spots. Here we extend this model to spherical wedge geometry covering the northern hemisphere up to 75° latitude and an azimuthal extent of 180°. The kinetic helicity and therefore also the large-scale magnetic field are strongest at low latitudes. For moderately strong stratification, several bipolar spots form that fill eventually the full longitudinal extent. At early times, the polarity of spots reflects the orientation of the underlying azimuthal field, as expected from  $\Omega$ -shaped flux loops. At late times their tilt changes such that there is a radial field of opposite orientation at different latitudes separated by about 10°. Our model demonstrates for the first time the spontaneous formation of spots of sizes much larger than the pressure scale height. Their tendency to produce filling factors close to unity is argued to be reminiscent of highly active stars. We confirm that strong stratification is an essential ingredient behind magnetic spot formation, which appears to be associated with downflows at larger depths.

*Subject headings:* Magnetohydrodynamics – turbulence – Sun: dynamo, activity

### 1. INTRODUCTION

Solar and stellar activity is characterized by the formation of magnetic spots. Sunspots are relatively small concentrations of magnetic field at the surface, where the radiation is suppressed significantly, making these regions cooler than their surroundings. Similar phenomena are also expected to occur on other stars exhibiting magnetic cycles, although the starspots observed so far all tend to be significantly larger than sunspots and not necessarily spatially correlated with the surface temperature (Kochukhov et al. 2013). There is little doubt that magnetic spots are associated with an underlying dynamo in the outer convection zones of these stars, but it is not clear whether they are caused by deeply rooted magnetic flux tubes at the bottom of the convection zones (Caligari et al. 1995), or whether they are merely shallow magnetic concentrations formed locally where the near-surface magnetic field exceeds a certain threshold. Magnetic field visualizations from convectively driven dynamo simulations have shown serpentine-shaped flux tubes that can be expected to intersect the surface (Nelson & Miesch 2014), but these tubes would expand during their ascent, so some sort of re-amplification of these tubes would be needed to explain sunspots.

The foundations of magnetic spot formation have been developed by Parker (1955), who identified magnetic buoyancy as the main agent responsible for bringing magnetic fields to the surface. In his subsequent work, Parker (1979) identified the need for a special mechanism to make these concentrations sufficiently cool and evacuated so as to explain the observed values of the magnetic field in sunspots. He postulated the existence of suitable downflows that would help to evacuate the magnetic flux

tube in its upper parts.

The appearance of such downdrafts in the region of spontaneously formed magnetic spots has been observed in the numerical simulations of Brandenburg et al. (2013) using forced turbulence with weak imposed vertical magnetic field. Downdrafts have also been seen in simulations of buoyantly rising flux tubes some time after they reached the surface (Rempel & Cheung 2014). A possible mechanism for producing such downdrafts might well be the negative effective magnetic pressure instability (NEMPI). It is based on the magnetic suppression of turbulent pressure so that, if the magnetic Reynolds number is larger than unity, the effective large-scale magnetic pressure (sum of turbulent and non-turbulent contributions) becomes negative and a large-scale instability (namely NEMPI) can be excited (Kleeorin et al. 1989, 1990, 1996; Kleeorin & Rogachevskii 1994; Rogachevskii & Kleeorin 2007). This instability can result in the formation of magnetic structures. As the work of recent years has shown, for horizontal magnetic fields, negative effective magnetic pressure leads to negative magnetic buoyancy at sub-equipartition field strengths (Brandenburg et al. 2010, 2011). However, for vertical fields the return flow replenishing the downflow occurs predominantly along magnetic field lines and has a much larger impact near the surface, where it can lead to super-equipartition strength flux concentrations (Brandenburg et al. 2013). Corresponding mean-field simulations (Brandenburg et al. 2014) have displayed great similarity with Parker's original picture (Parker 1979), where he explicitly stated the need for postulating the existence of downdrafts, leaving however the question about their origin open. On the other hand, the downflows have a strengths of only about 20% of the turbulent rms velocity and are therefore not easily recognized among

the downflows due to convection. Depending on circumstances, NEMPI can also lead to the formation bipolar spots (Warnecke et al. 2013) with super-equipartition field strengths (Mitra et al. 2014). The latter look remarkably similar to the bipolar regions found by Stein & Nordlund (2012) in realistic simulations of solar convection with an unstructured magnetic field being supplied at the bottom of their domain.

Strong stratification is a prerequisite for NEMPI to occur. In recent DNS of Mitra et al. (2014), it was demonstrated that stratification plays a role in the formation of magnetic spots that have surprisingly sharp boundaries with opposite polarities on the two sides. In these simulations, the turbulence in the deeper parts was made helical such that a large-scale magnetic field can be generated by the  $\alpha$  effect associated with the kinetic helicity of the turbulence. In the upper part of the domain in the DNS of Mitra et al. (2014) the turbulence forcing was non-helical, so there is no  $\alpha$  effect, but NEMPI can still work. What is surprising in those simulations is the fact that the magnetic fields in these structures exceeds the equipartition value by a factor of three or more. Since the effective magnetic pressure has not been measured in the simulations of Mitra et al. (2014), it is not obvious that the underlying mechanism is actually NEMPI, even though downflows with a strength of about 20% of the turbulent velocity could be detected. The physics of the formation of sharp magnetic edges of bipolar structures in the turbulent flow remains however elusive.

The magnetic field from the dynamo simulations of Mitra et al. (2014) had the property of extending over the entire horizontal length of the domain. As a consequence, only one bipolar structure was produced, which occasionally developed horizontal bands extending again over the full length of the horizontally periodic domain. To overcome this artifact of periodic boundary conditions, it is important to consider larger domains with either no or at least with physically motivated boundary conditions. A spherical shell is an obvious choice.

The dynamics of NEMPI from dynamo-generated magnetic fields in spherical shells or wedges has recently been studied by Jabbari et al. (2013) in a mean-field simulations (MFS), although in their case the dynamo mechanism operated throughout the domain and not just below a certain depth, as in the DNS of Mitra et al. (2014). Here we combine the two-layer setup of Mitra et al. (2014) with the shell geometry used in the MFS of Jabbari et al. (2013). There is also another DNS study by Jabbari et al. (2014) in which they investigated a combined system of dynamo and NEMPI in Cartesian geometry. In that paper, the combination of rotation and stratification leads to an  $\alpha^2$  dynamo. In the present work, we ignore rotation to understand first a simpler case using instead helically forced turbulence. Investigation of a similar system with rotation and shear will be the subject of a future study.

The purpose of the present paper is to study forced turbulence in a strongly stratified spherical shell. As in Mitra et al. (2014), the turbulence is made helical below a certain radius  $r_*$  so as to enable the formation of large-scale magnetic fields by the  $\alpha^2$  dynamo mechanism. The sign of the helicity is assumed to change across the equator. This leads to the formation of dynamo waves that travel toward the equator with opposite polarity in

the southern hemisphere (Mitra et al. 2010). This is a property that has been associated with the choice of perfectly conducting boundary conditions at high latitudes of the wedge. On the other hand, changing the high-latitude boundary condition to a normal field condition (often referred to as a vertical field condition) causes dynamo waves to propagate away from the equator and toward high latitudes, but now with the same polarity in both hemispheres (Brandenburg et al. 2009). In the present paper, we reconsider the former case and apply a suitable boundary condition at the equator to cut the computational costs.

There is another potential artifact of the dynamo waves of Mitra et al. (2010) in that they tend to occur at high latitudes where the kinetic helicity is assumed largest. On the other hand, we have seen in DNS of turbulent convection in spherical shells that kinetic helicity is in fact concentrated to regions outside the inner tangent cylinder of the shell (Käpylä et al. 2012b). This restricts the kinetic helicity essentially to low latitudes below  $45^\circ$ . We model this feature here by assuming a suitable profile for the kinetic helicity of the forcing function in the deeper parts of the shell.

## 2. THE MODEL

In this paper we investigate a system similar to that of Mitra et al. (2014), but in spherical geometry assuming either symmetric (quadrupolar) or anti-symmetric (dipolar) field properties about the equator. Jabbari et al. (2013) used MFS in spherical geometry to show how the large-scale dynamo can interact with NEMPI in such a coupled system. In their MFS, the mean-field Lorentz force was parameterized, which is subject to uncertainties. It is therefore useful to perform DNS and to study how the results depend on domain size, density stratification, geometry, and boundary conditions. As explained above, the main difference here is the fact that the forcing is not uniform in whole domain. As in Mitra et al. (2014), our domain is divided into two parts. We apply helical forcing (which leads to an alpha squared dynamo) in the lower part of the domain and non-helical forcing in the upper part of the domain. The position of the border between these two areas is varied to see how it affects the results. We expect to detect similar intense bipolar region of earlier DNS of Mitra et al. (2014).

We use an isothermal equation of state, so no convection is possible. Therefore, turbulence is driven using volume forcing given by a function  $f$  that is  $\delta$ -correlated in time and monochromatic in space. It consists of random non-polarized waves whose direction and phase change randomly at each time step. We present a more detailed discussion about forcing in §2.2.

### 2.1. Basic equations

In DNS of an isothermally stratified layer we solve the equations for the velocity  $\mathbf{U}$ , the magnetic vector potential  $\mathbf{A}$ , and the density  $\rho$ ,

$$\rho \frac{D\mathbf{U}}{Dt} = \mathbf{J} \times \mathbf{B} - c_s^2 \nabla \rho + \nabla \cdot (2\nu \rho \mathbf{S}) + \rho(\mathbf{f} + \mathbf{g}), \quad (1)$$

$$\frac{\partial \mathbf{A}}{\partial t} = \mathbf{U} \times \mathbf{B} + \eta \nabla^2 \mathbf{A}, \quad (2)$$

$$\frac{\partial \rho}{\partial t} = -\nabla \cdot \rho \mathbf{U}, \quad (3)$$

where the operator  $D/Dt = \partial/\partial t + \mathbf{U} \cdot \nabla$  is the advective derivative,  $\eta$  is the magnetic diffusivity,  $\mathbf{B} = \nabla \times \mathbf{A}$  is the magnetic field,  $\mathbf{J} = \nabla \times \mathbf{B}/\mu_0$  is the current density,  $\mathbf{S}_{ij} = \frac{1}{2}(U_{i,j} + U_{j,i}) - \frac{1}{3}\delta_{ij}\nabla \cdot \mathbf{U}$  is the traceless rate of strain tensor (the commas denote partial differentiation),  $\nu$  is the kinematic viscosity,  $c_s$  is the isothermal sound speed, and  $\mu_0$  is the vacuum permeability. We adopt spherical coordinates  $(r, \theta, \phi)$ .

For the  $\phi$  direction we use periodic boundary conditions. In the radial direction (the direction of the stratification), we consider perfectly conducting boundary conditions at the bottom and a vertical field boundary condition at the top. At the equator, we adopt a symmetry condition such that the magnetic field is either symmetric (quadrupolar) or anti-symmetric (dipolar) with respect to the equator. For the magnetic field we assume perfect conductor boundary conditions on the latitudinal ( $\theta = \theta_0$ ) and lower radial ( $r = r_0$ ) boundaries, and radial field boundary conditions on the outer radius ( $r = R$ ). On the equator, we assume either dipolar or a quadrupolar symmetry. In terms of the magnetic vector potential these conditions translate to

$$\frac{\partial A_r}{\partial r} = A_\theta = A_\phi = 0 \quad (r = r_0), \quad (4)$$

$$A_r = 0, \quad \frac{\partial A_\theta}{\partial r} = -\frac{A_\theta}{r}, \quad \frac{\partial A_\phi}{\partial r} = -\frac{A_\phi}{r} \quad (r = R), \quad (5)$$

$$A_r = \frac{\partial A_\theta}{\partial \theta} = A_\phi = 0 \quad (\theta = \theta_0, \pi/2) \quad (6)$$

for quadrupolar symmetry and

$$\frac{\partial A_r}{\partial \theta} = A_\theta = \frac{\partial A_\phi}{\partial \theta} = 0 \quad (\theta = \pi/2) \quad (7)$$

for dipolar symmetry.

For the velocity field we use stress-free, non-penetrating boundary conditions in the radial direction. The gravitational acceleration is  $\mathbf{g} = -\nabla\Phi$ , where

$$\Phi(r) = -GM \left( \frac{1}{r} - \frac{1}{r_m} \right). \quad (8)$$

Here  $G$  is Newton's constant and  $M$  is the mass of the sphere (or star). For an isothermal gas, the hydrostatic density stratification obeys  $\rho = \rho_0 \exp(-\Phi/c_s^2)$ , where  $\rho = \rho_0$  is the density in the middle of the shell at  $r = r_m = (r_0 + R)/2$ . The radial component of the gravitational acceleration is then  $g = -GM/r^2$ . The quantity  $GM$  determines the density contrast  $\Gamma_\rho = \rho_{\text{bot}}/\rho_{\text{top}}$  between bottom and top of the domain. The thickness of the shell is  $\Delta r = R - r_0$ , and it is used to define a reference wavenumber  $k_1 = 2\pi/\Delta r$ .

## 2.2. The forcing function

The forcing function  $\mathbf{f}$  is similar to that of Mitra et al. (2014),

$$\mathbf{f}(\mathbf{x}, t) = \text{Re} \left[ N \tilde{\mathbf{f}}(\mathbf{k}, t) \exp(i\mathbf{k} \cdot \mathbf{x} + i\varphi) \right], \quad (9)$$

where  $\mathbf{x}$  is the position vector,  $-\pi < \varphi \leq \pi$  is a randomly selected phase, and  $\mathbf{k}$  is the wavevector which is chosen

from a set of wavevectors in a certain range around a given forcing wavenumber,  $k_f$ . The Fourier amplitudes,

$$\tilde{\mathbf{f}}(\mathbf{k}) = \mathbf{R} \cdot \tilde{\mathbf{f}}(\mathbf{k})^{(\text{nohel})} \quad \text{with} \quad \mathbf{R}_{ij} = \frac{\delta_{ij} - i\sigma\epsilon_{ijk}\hat{\mathbf{k}}}{\sqrt{1 + \sigma^2}}, \quad (10)$$

where  $\sigma$  characterizes the fractional helicity of  $\mathbf{f}$ , and

$$\tilde{\mathbf{f}}(\mathbf{k})^{(\text{nohel})} = (\mathbf{k} \times \hat{\mathbf{e}}) / \sqrt{\mathbf{k}^2 - (\mathbf{k} \cdot \hat{\mathbf{e}})^2} \quad (11)$$

is a non-helical forcing function, and  $\hat{\mathbf{e}}$  is an arbitrary unit vector not aligned with  $\mathbf{k}$  and  $\hat{\mathbf{k}}$  is the unit vector along  $\mathbf{k}$ ; note that  $|\tilde{\mathbf{f}}|^2 = 1$ . The degree of helicity is modulated in space via the function

$$\sigma(r, \theta) = \frac{\sigma_{\text{max}}}{2} \left[ 1 - \text{erf} \left( \frac{r - r_*}{w_f} \right) \right] \cos \theta \sin^n \theta, \quad (12)$$

where erf is the error function,  $r_*$  is the radius above which the helicity vanishes,  $w_f$  is the width of the transition layer, and the exponent  $n$  determines the latitudinal helicity profile. We choose  $w_f = 0.01$  for all the simulations. For more details of this type of forcing see Mitra et al. (2014).

## 2.3. Parameters of the simulations

During the exponential growth phase of the dynamo, the growth rate is calculated as  $\lambda = dB_{\text{rms}}/dt$ . The nondimensional growth rate is given as  $\tilde{\lambda} = \lambda/u_{\text{rms}}k_f$ . However, the time of the simulation is normally specified in terms of the turbulent-diffusive time  $\tau_{\text{td}} = (\eta_{\text{t0}}k_1^2)^{-1}$ , where  $\eta_{\text{t0}} = u_{\text{rms}}/3k_f$  is the estimated turbulent diffusivity. In most of the calculations, we use a scale separation ratio  $k_f/k_1$  of 30 and a fluid Reynolds number  $\text{Re} \equiv u_{\text{rms}}/\nu k_f$  of 20. Our magnetic Prandtl number  $\text{Pr}_M = \nu/\eta$  is 1, so the magnetic Reynolds number is then  $\text{Re}_M = \text{Pr}_M \text{Re} = 20$ . These values are chosen to have both  $k_f$  and  $\text{Re}$  large enough for NEMPI to develop at an affordable numerical resolution. The magnetic field is expressed in units of local equipartition magnetic field,  $B_{\text{eq}}(r) = \sqrt{\mu_0 \bar{\rho}(r) u_{\text{rms}}}$ , where  $\bar{\rho}(r)$  is the density averaged over time and spherical shells. We also define  $B_{\text{eq0}} = \sqrt{\mu_0 \rho_0} u_{\text{rms}}$ . In the following, we use nondimensional units by setting  $c_s = \mu_0 = \rho_0 = 1$ .

We perform simulations with density contrasts between 2 and 1400. This enables us to study the effect of stratification on the formation of magnetic structures. For most of the simulations, we choose  $n = 6$  in Equation (12), i.e., the helicity is maximum at lower latitudes. This is also the case for our two reference runs, which have  $\Gamma_\rho = 450$  and either quadrupolar or dipolar parity. However, for comparison we also present cases where  $n = 0$ .

We use the PENCIL CODE<sup>1</sup> to perform direct numerical simulations. This code uses sixth-order explicit finite differences in space and a third-order accurate time-stepping method. We use  $r_0 = 0.7R$  and  $\theta_0 = 15^\circ$ . For runs with a  $\phi$  extend of  $\pi$ , we use a numerical resolution of  $256 \times 1152 \times 1152$  mesh points in the  $r$ ,  $\theta$ , and  $\phi$  directions, and  $256 \times 1152 \times 288$  for all other runs. Table 1 shows all runs with their parameters.

<sup>1</sup> <http://pencil-code.googlecode.com>

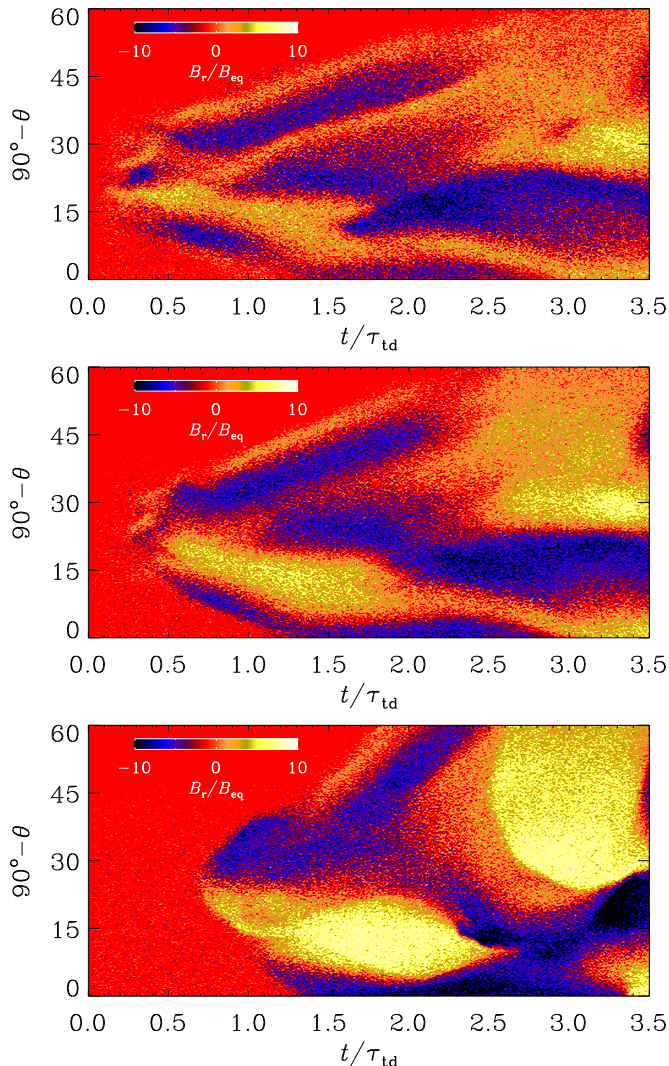


FIG. 1.— Butterfly diagram for our reference run (Run Q2 with  $\Gamma_\rho = 450$ ) at  $r/R = 0.75$  (top),  $0.8$  (middle), and  $0.95$  (bottom).

TABLE 1

SUMMARY OF THE RUNS. THE REFERENCE RUN IS SHOWN IN BOLD.

Run	$\Gamma_\rho$	$r_*$	$\phi$ ext.	$\text{Re}_M$	$n$	b.c.	$\sigma_{\max}$	$\bar{\lambda}$
Q1	2	0.8	$\pi$	20	6	Q	1	0.079
<b>Q2</b>	<b>450</b>	<b>0.8</b>	<b><math>\pi</math></b>	<b>20</b>	<b>6</b>	<b>Q</b>	<b>1</b>	<b>0.084</b>
Q3	1400	0.8	$\pi$	20	6	Q	1	0.04
Q4	450	0.75	$\pi$	20	6	Q	1	0.074
D1	2	0.8	$\pi$	20	6	D	1	0.087
<b>D2</b>	<b>450</b>	<b>0.8</b>	<b><math>\pi</math></b>	<b>20</b>	<b>6</b>	<b>D</b>	<b>1</b>	<b>0.082</b>
D3	1400	0.8	$\pi$	20	6	D	1	0.077
D4	450	0.8	$\pi$	20	6	D	0.2	0.11
R1	450	0.8	$\pi/4$	20	6	D	1	0.0083
R2	450	0.8	$\pi/4$	40	6	D	1	0.075
H1	2	0.8	$\pi$	20	0	Q	1	0.087
H2	450	0.8	$\pi$	20	0	Q	1	0.083
H3	1400	0.8	$\pi$	20	0	Q	1	0.076
H4	450	0.75	$\pi$	20	0	Q	1	0.081

NOTE. — The column ‘b.c.’ indicates whether the equatorial boundary condition is dipolar (D) or quadrupolar (Q).

### 3. RESULTS

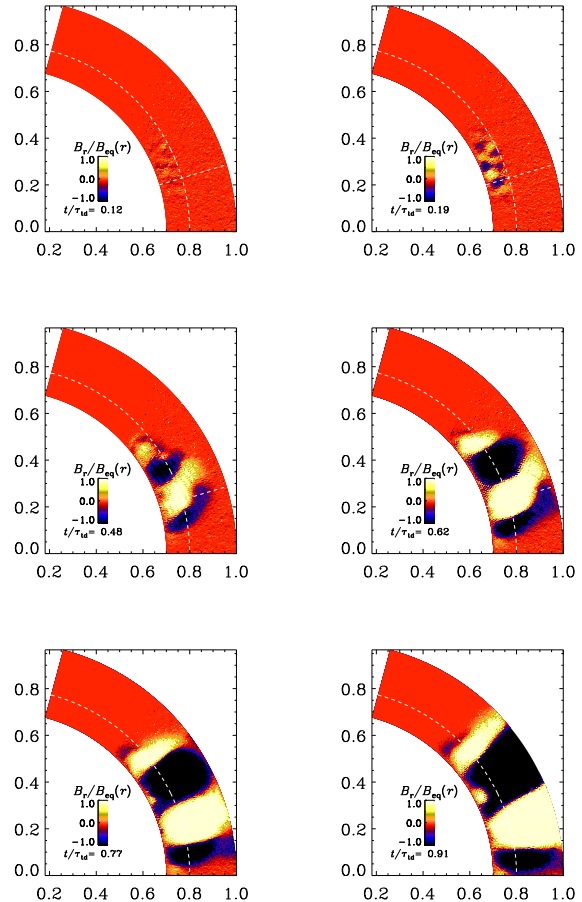


FIG. 2.— Meridional cross-sections of  $\bar{B}_r/B_{\text{eq}}$  at different times for Run Q2.

#### 3.1. Nature of the dynamo

Mean-field simulations of  $\alpha^2$  dynamos in spherical shell wedges have shown that the magnetic field is strongest near the high-latitude boundaries (Jabbari et al. 2013). However, in rapidly rotating stratified spherical shell convection, the kinetic helicity is typically found to be maximum close to the equator, e.g. at  $\pm 15^\circ$  latitude (Käpylä et al. 2012b). For this reason, we focus in the present paper on the case  $n = 6$ , which yields a maximum of the magnetic field at about  $22^\circ$ .

In Figure 1 we show butterfly diagrams of  $B_r(\theta, t)/B_{\text{eq}}$  at  $r/R = 0.75, 0.8$ , and  $0.95$  and  $\phi = 0$ . We observe equatorward migration of the magnetic field at low latitudes (below  $20^\circ$ ) and poleward migration at higher ones.

The observed dynamo wave is generated by an  $\alpha^2$  dynamo. The fact that  $\alpha^2$  dynamos with nonuniform  $\alpha$  distribution can be oscillatory was known for some time (Shukurov et al. 1985; Baryshnikova & Shukurov 1987; Stefani & Gerbeth 2005), but their migratory properties were first pointed out by Mitra et al. (2010). Not surprisingly, the magnetic field is generated in the lower layer, as can be seen from Figure 2 where we show meridional cross-sections of  $B_r(r, \theta)/B_{\text{eq}}(r)$  at  $\phi = 0$  at six different times.

We note that during the early growth phase of the dynamo, the magnetic field grows exponentially and the

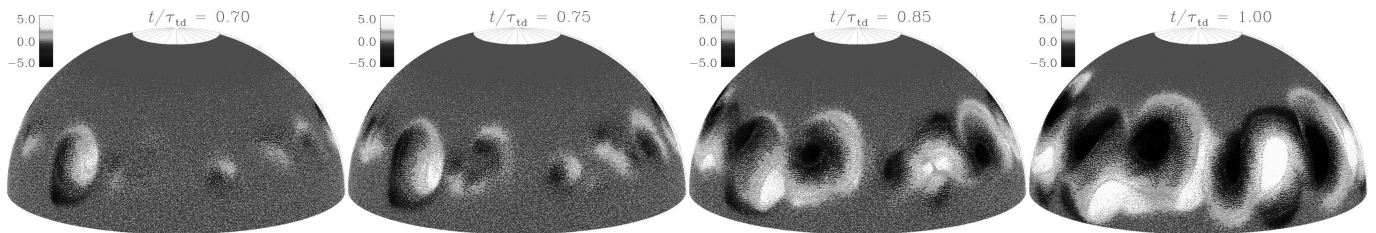


FIG. 3.— Time evolution of  $B_r/B_{\text{eq}}$  at  $r/R = 0.98$  for a simulation with  $\Gamma_\rho = 450$  for Run Q2.

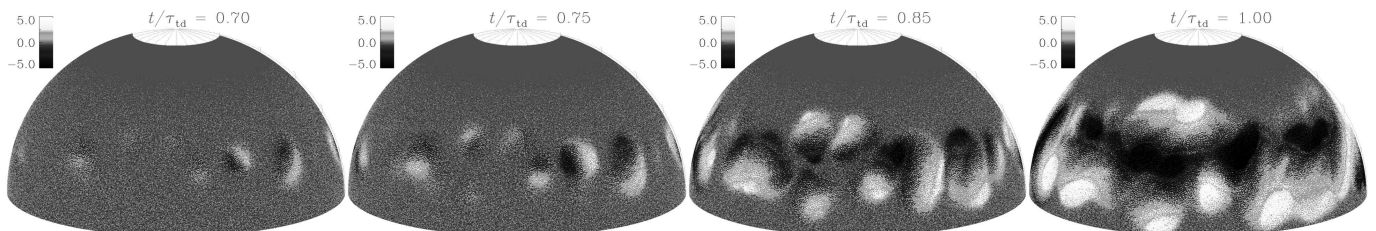


FIG. 4.— Same as Figure 3, but for Run D2.

non-dimensional growth rate is of the order of 0.1. It increases with magnetic Reynolds number (cf. Runs R1 and R2), which might be related to the possibility of small-scale dynamo action. This is supported by the fact that the growth rate is not increasing with helicity (cf. Runs D2 and D4).

### 3.2. Spot formation

Next, we consider the surface appearance of the radial magnetic field. We see the formation of structures at low latitudes in less than a turbulent diffusive time. At first a few bipolar regions form. As time goes on, these structures move, rotate, and expand, and after a long enough time they form a strong field concentration which move toward the equator and forms three band-like structures with opposite polarities (see Figure 4). A similar behavior was also observed by Mitra et al. (2014); see Figures 3 and 4 of their paper.

Figures 3 and 4 illustrate the time evolution of our reference simulations (Runs Q2 and D2) with  $\Gamma_\rho = 450$ . As one can see, at early times of bipolar spot formation, the two polarities are very close to each other. One sees that each polarity consists of a core with strong field and a shadow around it with weaker field. As time elapses, both core and the shadow expand but the speed of the expansion of the shadow is larger than the speed of expansion of the core. This implies that two polarities start moving apart from each other. The rest of the evolution is somewhat different for Runs Q2 and D2. For Run Q2, the bipolar spot orientation is preferentially in the azimuthal direction, both at early and later times. For Run D2, on the other hand, the spots tilt in such a way that the part of the structure with the same polarity tends to occupy a certain latitudinal band, while that of the opposite orientation occupies a band at a different latitude; see Figure 4. This global structure remains without change, no matter how much time passes.

The time dependence of magnetic energy and its radial profile are shown in Figure 5. Different colors correspond to different degree of stratification. Earlier studies have

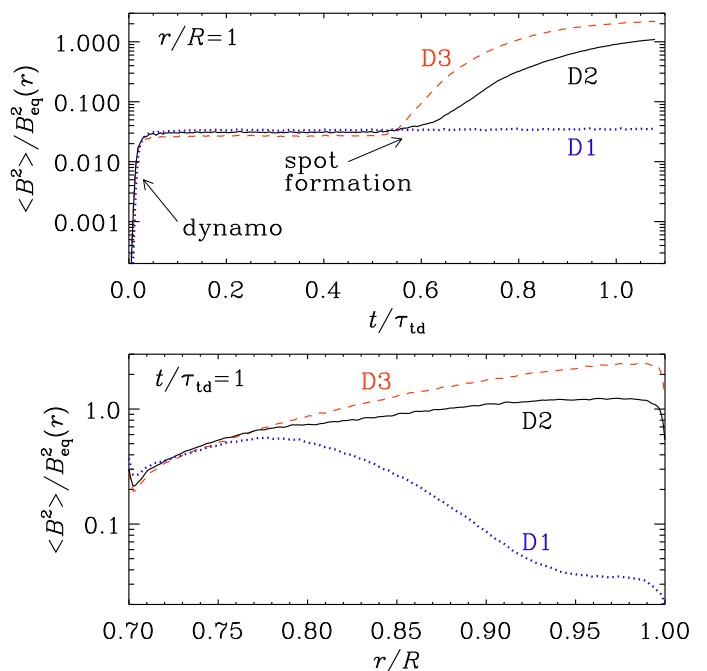


FIG. 5.— Upper panel: time evolution of  $\langle B^2 \rangle / B_{\text{eq}}^2(r)$  for runs D1 (dotted, blue), D2 (solid, black), and D3 (dashed, red). Lower panel: radial dependence of  $\langle B^2 \rangle / B_{\text{eq}}^2(r)$  for  $t/\tau_{\text{td}} = 1$  for Runs D1–D3.

demonstrated the importance of stratification in the formation of structures through NEMPI. In fact, by increasing the stratification, the structures were found to be more intense. For the highest stratification ( $\Gamma_\rho = 1400$ ), the total magnetic energy becomes somewhat larger than for  $\Gamma_\rho = 450$ , although the strength of the spots is about equally strong. This suggests that, there might be an upper limit for the density contrast. A similar effect was also observed in the work of Jabbari et al. (2014), which they referred to it as gravitational quenching, which suppresses NEMPI. We must also remember that NEMPI

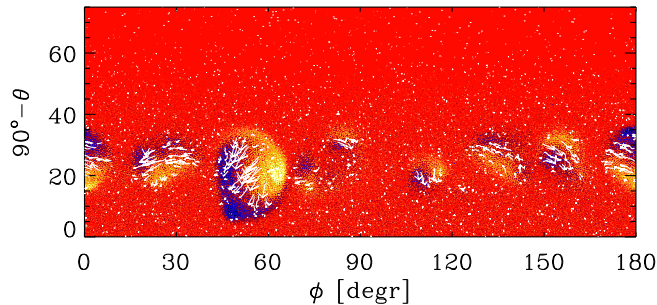


FIG. 6.— Mercator projection of  $B_r/B_{\text{eq}}$  with  $(B_\theta, B_\phi)$  vectors superimposed just below the surface at  $t/\tau_{\text{td}} = 0.7$  for Run Q2.

can only work in regions where the magnetic field relative to the equipartition value is in the optimal range (Kemel et al. 2012; Losada et al. 2014; Brandenburg et al. 2014). However, in our strongly stratified system, the regions where this would be the case can become rather narrow. This gives another geometric constraint on the possibility of NEMPI, which was already discussed by Losada et al. (2014) in connection with polytropic stratifications, where this limitation can become particularly severe. Further studies are needed to understand the origin of this effect.

### 3.3. Inclination angle

Our spots show a systematic East-West orientation with negative vertical field on the left and positive values on the right. In addition, some of the regions also show a certain tilt, although the apparent yin-yang structure makes it hard to say whether the tilt angle is positive or negative. Most of the bipolar regions are oriented in a similar fashion, although there is also a large fraction of spots that show random orientation. Parker (1955) suggested that sunspot pairs are produced by the buoyant rise of a flux tube, which takes the form of an  $\Omega$  loop near the surface. To see whether this is also the case in the present simulations, we show in Figure 6  $B_r/B_{\text{eq}}$  at the surface together with field vectors projected onto the horizontal plane. Note that the vectors tend to point in the negative  $\phi$  direction, i.e., the azimuthal field points to the left. In most of the bipolar spots in this figure,  $B_r/B_{\text{eq}}$  tends to be positive on the right-hand side of the spot (pointing upward) and negative on the left-hand side of the spot (pointing downward). This corresponds to the expected  $\Omega$  loop scenario.

### 3.4. Dependence on $r_*$ , $\sigma$ , Reynolds number, stratification, and scale separation

We recall that we adopt a similar forcing setup as Mitra et al. (2014) with a transition at a radius  $r_*$  from helical forcing in the deeper parts to non-helical in the upper parts. Mitra et al. (2014) found that, when the border is moved closer to the bottom of the convection zone, the structures appear later. This is due to the fact that it takes a longer time for dynamo to affect the upper layers. A similar behavior was observed when the helicity parameter  $\sigma$  is decreased from its maximum value of 1. In such a case the formation of structures occurs again with time delay, which is due to the weaker dynamo. However, the present simulations show that the dynamo growth rate does even slightly increase with decreasing helicity; cf. Runs D2 and D4. On the other hand, lowering the value

of  $r_*$  does lead to a small decrease of the growth rate; cf. Runs Q2 and Q4 as well as Runs H2 and H4.

The effect of stratification on the formation of the spot is shown in Figure 7. For the lowest density contrast, no structures form, independently of time, size of the shell, value of Reynolds number, and position of the border between helical and non-helical turbulence. This confirms that stratification plays a crucial role in the formation of bipolar regions.

In spherical geometry, it is possible to investigate the effect of different  $\phi$  extent on the formation of structures. Not surprisingly, it turns out that for small  $\phi$  extent (below  $\pi/6$ ) the size of the spots is limited by the domain size.

### 3.5. Effective magnetic pressure

To assess whether NEMPI is operating, we now calculate the effective magnetic pressure, following Brandenburg et al. (2012) and adapting the formulation to the spherical case. Using the  $\theta\theta$ - and  $\phi\phi$ -components of the total stress from fluctuating velocity and magnetic fields, one gets

$$\Delta\bar{\Pi}_i^f = \bar{\rho}(\overline{u_i^2} - \overline{u_{0i}^2}) + \frac{1}{2}(\overline{b^2} - \overline{b_0^2}) - (\overline{b_i^2} - \overline{b_{0i}^2}), \quad (13)$$

where the subscript  $i$  refers to either  $\theta$  or  $\phi$ . The subscript 0 refers to the case with zero magnetic field. But as the background field is here dynamo generated, we use the values of the related quantities in the upper part of the domain (non-helical part) at early times. This gives us the possibility to estimate the effective magnetic pressure in spherical geometry with dynamo-generated magnetic field. In Equation (13),  $\Delta\bar{\Pi}_i^f$  denotes the three diagonal components of the tensor  $\Delta\bar{\Pi}_{ij}^f$ . In the mean-field description, it depends on the mean magnetic field  $\bar{\mathbf{B}}$  and is parameterized as

$$\Delta\bar{\Pi}_{ij}^f = \left( q_s \hat{\beta}_i \hat{\beta}_j - \frac{1}{2} q_p \delta_{ij} + q_g \hat{g}_i \hat{g}_j \right) \bar{\mathbf{B}}^2, \quad (14)$$

where  $\hat{\beta}_i$  and  $\hat{g}_i$  are the unit vectors along  $\bar{\mathbf{B}}$  and  $\mathbf{g}$ , respectively. The effective magnetic pressure is defined as a sum of non-turbulent and turbulent contributions:

$$\mathcal{P}_{\text{eff}} = \frac{1}{2}(1 - q_p)\beta^2, \quad (15)$$

where,  $q_p$  is

$$q_p = -\frac{1}{\bar{\mathbf{B}}^2} [\Delta\bar{\Pi}_\theta + \Delta\bar{\Pi}_\phi - q_s(\bar{B}_\theta^2 + \bar{B}_\phi^2)], \quad (16)$$

with

$$q_s = (\Delta\bar{\Pi}_\theta - \Delta\bar{\Pi}_\phi) / (\bar{B}_\theta^2 - \bar{B}_\phi^2), \quad (17)$$

and

$$q_g = \frac{1}{\bar{\mathbf{B}}^2} \left[ -\Delta\bar{\Pi}_r + q_s \bar{B}_r^2 - \frac{1}{2} q_p \bar{\mathbf{B}}^2 \right]. \quad (18)$$

Previous studies (Brandenburg et al. 2012; Käpylä et al. 2012a) in Cartesian geometry have shown that  $q_s$  and  $q_g$  are very close to zero. This is also confirmed by the present simulations, where  $\Delta\bar{\Pi}_\theta - \Delta\bar{\Pi}_\phi$  is found to correlate poorly with  $\bar{B}_\theta^2 - \bar{B}_\phi^2$ . We therefore ignore  $q_s$  and  $q_g$  in most of the following.

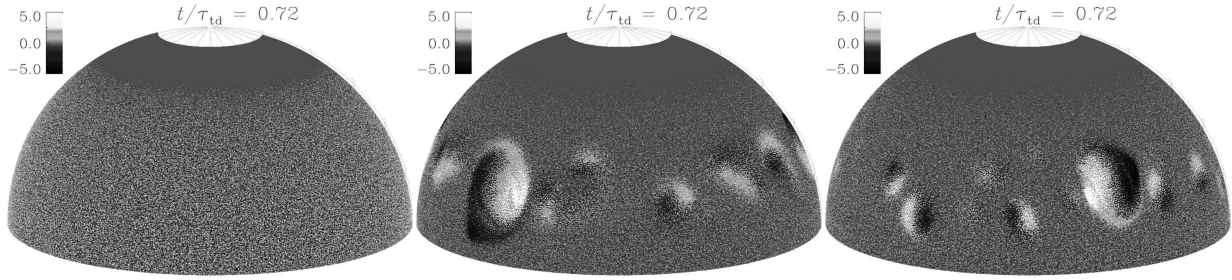


FIG. 7.—  $B_r/B_{\text{eq}}$  for simulations with different stratifications for Runs Q1, Q2 and Q3 with density contrasts 2, 450 and 1400 from left to the right, respectively.

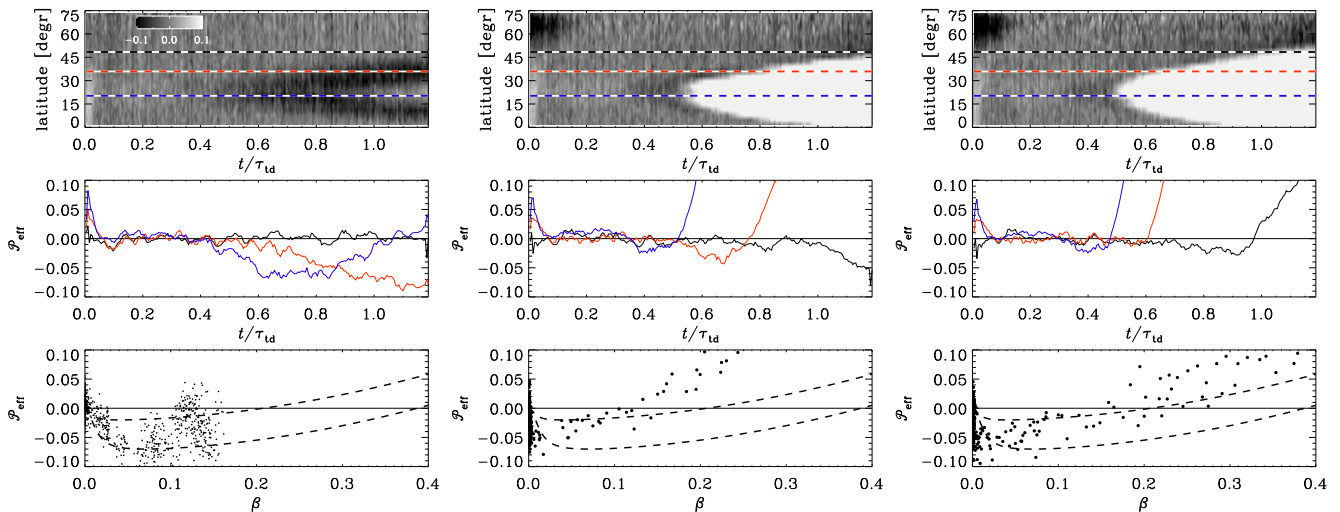


FIG. 8.—  $\mathcal{P}_{\text{eff}}$  vs.  $t$  and  $\theta$  for  $r/R = 0.85$  in the top panels, for  $\Gamma_\rho = 2$  (left), 450 (middle column), and 1400 (right). The horizontal lines in black, red, and blue indicate three latitudes ( $50^\circ$ ,  $35^\circ$ , and  $20^\circ$ ), for which we show  $\mathcal{P}_{\text{eff}}$  vs.  $t$  in the middle panels. The bottom panels show scatter plots of  $\mathcal{P}_{\text{eff}}(\beta)$ .

Next, we subtract the time average of an early time interval between times  $t_1$  and  $t_2$  and compute the diagonal components of the change of the stress as

$$\Delta \bar{\Pi}_i(r, \theta, t) = \bar{\Pi}_i(r, \theta, t) - \frac{1}{t_2 - t_1} \int_{t_1}^{t_2} \bar{\Pi}_i(r, \theta, t') dt', \quad (19)$$

where  $t_1 = 0.1\tau_{\text{td}}$  and  $t_2 = 0.5\tau_{\text{td}}$  denote the time interval over which the stratification is not yet affected by the magnetic field. We thus compute

$$q_p = -(\Delta \bar{\Pi}_\theta + \Delta \bar{\Pi}_\phi) / \bar{B}^2, \quad (20)$$

so we get  $\mathcal{P}_{\text{eff}} = \frac{1}{2}(1 - q_p)\beta^2$ , where  $\beta^2 = \bar{B}^2 / B_{\text{eq}}^2(r, \theta, t)$ .

In Figure 8 we show  $\mathcal{P}_{\text{eff}}$  vs.  $t$  and  $\theta$  for  $r/R = 0.85$  using Runs Q1, Q2, and Q3. The bottom panels show scatter plots of  $\mathcal{P}_{\text{eff}}(\beta)$ . It is customary to fit such data to an expression of the form (Kemel et al. 2012)

$$q_p(\beta) = \beta_*^2 / (\beta_p^2 + \beta^2), \quad (21)$$

where  $(\beta_*, \beta_p)$  is a set of fit parameters. They have previously been determined for Cartesian simulations with an imposed magnetic field (Brandenburg et al. 2012). In Figure 8, the dashed lines show for comparison the result for two representations of Equation (21) with  $(\beta_*, \beta_p) = (0.39, 0.013)$  and  $(0.21, 0.008)$  for curves with

the deeper and less deep minimum, respectively. Neither of the curves fit the data points well. Nevertheless, it is important to note that  $\mathcal{P}_{\text{eff}}$  is always negative for  $\beta < 0.1$ , although in the runs with stronger stratification the number of such points is rather small.

Thus, we may conclude that, although there is evidence for negative values of  $\mathcal{P}_{\text{eff}}$ , we can still not be certain that NEMPI really does play a sufficiently significant role to explain the occurrence of spots in our simulations. Furthermore, the relatively sharp boundary of our spots, which is a marked feature of these types of calculation, is probably related to mean-field terms in the induction equation rather than the momentum equation.

In the near-surface layers, on the other hand, there is no evidence for negative effective magnetic pressure, as can be seen from Figure 9, where we show the results for  $\mathcal{P}_{\text{eff}}$  at  $r/R = 0.98$  and for  $\Gamma_\rho = 450$ . This is however consistent with the idea that spots are formed mainly due to suction from deeper layers (Brandenburg et al. 2014).

To check whether there are downflows at greater depth where NEMPI can act, we compare in Figure 10 for Run D2 contours of negative and positive vertical velocity,  $\langle U_r \rangle_{kR < 50}$ , superimposed on a gray-scale representation of  $\langle B_r \rangle_{kR < 100}^2 / B_{\text{eq}}^2(r)$  at  $r/R = 0.85$ . Here,  $\langle \cdot \rangle_{kR}$  denotes Fourier filtering, applied to obtain smoother con-

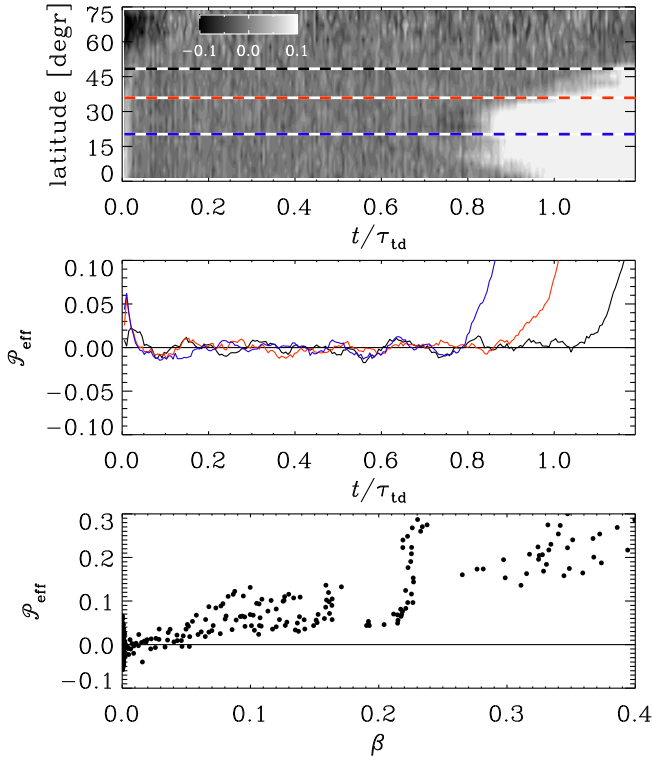


FIG. 9.— Similar to Figure 8, but for  $r/R = 0.98$  and for  $\Gamma_\rho = 450$ .

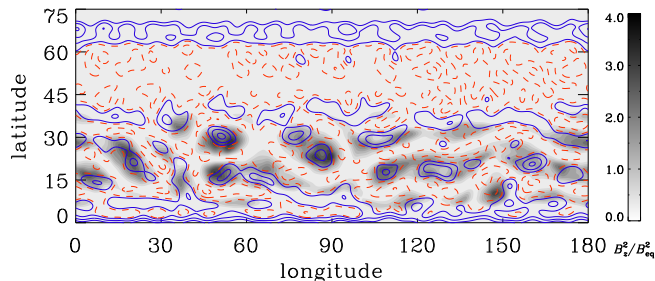


FIG. 10.— Contours of negative (blue, solid lines) and positive (red, dashed) vertical velocity  $\langle U_r \rangle_{kR < 50}$  superimposed on a grayscale representation of  $\langle B_r \rangle_{kR < 100}^2 / B_{\text{eq}}^2(r)$  in Mercator projection at  $r/R = 0.85$  and  $t/\tau_{td} = 0.7$ .

tours. (For  $B_r$  we also apply some filtering, but only above  $kR = 100$  to eliminate patterns on the scale of the forcing.) We see that there are indeed many places where the field is strong and  $\langle U_r \rangle_{kR < 50}$  is negative, but the correlation is not very strong. Furthermore, since the field strength exceeds the equipartition value even at this greater depth, NEMPI must have seized to work. Nevertheless, it could have operated at earlier times when the field was weaker.

Finally, a comment regarding the possible importance of the  $q_s$  term is in order. As we have mentioned above,  $q_s$  cannot be determined owing to the poor correlation between  $\Delta \bar{\Pi}_\theta - \Delta \bar{\Pi}_\phi$  and  $\bar{B}_\theta^2 - \bar{B}_\phi^2$ . However, at  $r/R = 0.85$  and near  $35^\circ$  latitude, the correlation is not quite as poor and  $q_s$  can be determined in the time interval  $0.7 < t/\tau_{td} < 0.85$ , where  $q_s \approx 20$  is found. On the other hand, in the neighborhood of this latitude,  $q_s$  turns out

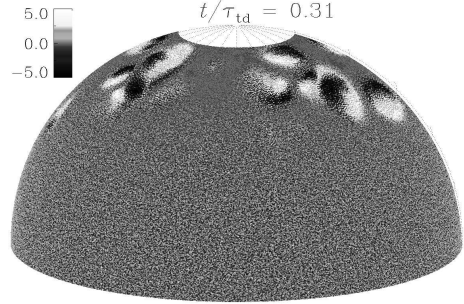


FIG. 11.— Formation of the high-latitude spots for the case  $n = 0$  (Run H2).

to be in the range  $0 < q_s < 20$ . The corresponding values of  $q_g$  are found to be in the range from  $-5$  to  $10$ . Furthermore, if the  $q_s$  term in Equation (18) were ignored, we find values in the range  $-5 < q_g < 0$ . Interestingly, mean-field simulations of NEMPI have shown earlier that values in the range  $-10 < q_g < 10$  do not significantly affect the growth rate (Käpylä et al. 2012a), suggesting that  $q_g$  remains subdominant, regardless of whether or not the  $q_s$  term is taken into account.

### 3.6. High-latitude spots

Before concluding, let us return once more to the occurrence of magnetic spots and its dependence on the parameter  $n$  in Equation (12). When the helicity is large at high latitudes, i.e., when we choose the helicity profile with  $n = 0$ , magnetic spots are found to form close to the poles in a fashion reminiscent of recent simulations by Yadav et al. (2014). Figure 11 presents the formation of spots near the pole for run H2. The results of the simulations with  $n = 0$  show similar behavior and parameter dependence as the case with  $n = 6$ . As for  $n = 6$ , for weaker stratification no spots form and for smaller  $\sigma$  and deeper  $r_*$ , the structures form with a time delay.

## 4. CONCLUSIONS

The present work has demonstrated that in a strongly stratified two-layer spherical model with helical turbulence in the lower layer and non-helical turbulence in the upper one, the  $\alpha^2$  dynamo produces large-scale magnetic fields that develop sharp spot-like structures at the surface. This confirms the results of Mitra et al. (2014) in Cartesian geometry, but now for a much larger domain. We therefore see for the first time that the bipolar magnetic spots have a finite size. However, contrary to earlier expectations (Kemel et al. 2012; Brandenburg et al. 2014), the size of these structures exceeds the local value of the density scale height by much more than the earlier expected value of about ten.

In our present simulations the dynamo (caused by the  $\alpha^2$  dynamo) is fully helical, so the resulting large-scale field is rather strong and the magnetic spots begin to fill eventually the entire horizontal surface. This is also what is expected for very active stars where the filling factor of the surface magnetic field is known to reach unity as the star becomes more active (Saar & Linsky 1985). Conversely, to model sunspots, which are much smaller, we expect that we would need to decrease the fractional helicity.

The physics behind spot formation remains still somewhat obscure. While it is clear that strong stratification is an essential element behind spot formation, the results presented here do not match our earlier findings that were obtained under more idealizing conditions such as the use of an imposed magnetic field. However, like the earlier results of Mitra et al. (2014) we find again evidence for downflows below the sites of spot formation and, in particular, the formation of sharply bounded structures. The latter is reminiscent of the appearance of sharp structures as a result of ambipolar diffusion under laminar conditions (Brandenburg & Zweibel 1994). This raises the question, whether for strongly stratified turbulence the effective magnetic diffusivity can attain a nonlinear dependence on the magnetic field that is similar to that of ambipolar diffusion, i.e., it increases with increasing field strength. To address these questions, it would be best to return to Cartesian geometry where it would be possible to determine turbulent transport coefficients with dedicated methods such as the test-field ap-

proach. This is however beyond the scope of the present work.

This work was supported in part by the Swedish Research Council Grants No. 621-2011-5076 and 2012-5797, the Research Council of Norway under the FRINATEK grant 231444, the Academy of Finland under the ABBA grant No. 280700, Russian Federal Program under the grant No. 14.578.21.0033, as well as the Government of the Russian Federation under a mega-grant 11.G34.31.0048. We acknowledge the allocation of computing resources provided by the Swedish National Allocations Committee at the Center for Parallel Computers at the Royal Institute of Technology in Stockholm and the National Supercomputer Centers in Linköping, the High Performance Computing Center North in Umeå, and the Nordic High Performance Computing Center in Reykjavik.

#### REFERENCES

- Baryshnikova, I., & Shukurov, A., 1987, *Astron. Nachr.*, 308, 89  
 Brandenburg, A., & Zweibel, E. G. 1994, *ApJ*, 427, L91  
 Brandenburg, A., Candelaresi, S., & Chatterjee, P. 2009, *MNRAS*, 398, 1414  
 Brandenburg, A., Gressel, O., Jabbari, S., Kleeorin, N., & Rogachevskii, I. 2014, *A&A*, 562, A53  
 Brandenburg, A., Kemel, K., Kleeorin, N., Mitra, D., Rogachevskii, I. 2011, *ApJ*, 740, L50  
 Brandenburg, A., Kemel, K., Kleeorin, N., Rogachevskii, I. 2012, *ApJ*, 749, 179  
 Brandenburg, A., Kleeorin, N., & Rogachevskii, I. 2010, *Astron. Nachr.*, 331, 5  
 Brandenburg, A., Kleeorin, N., & Rogachevskii, I. 2013, *ApJ*, 776, L23  
 Caligari, P., Moreno-Insertis, F., & Schüssler, M. 1995, *ApJ*, 441, 886  
 Jabbari, S., Brandenburg, A., Kleeorin, N., Mitra, D., & Rogachevskii, I. 2013, *A&A*, 556, A106  
 Jabbari, S., Brandenburg, A., Losada, I. R., Kleeorin, N., & Rogachevskii, I. 2014, *A&A*, 568, A112  
 Käpylä, P. J., Brandenburg, A., Kleeorin, N., Mantere, M. J., & Rogachevskii, I. 2012a, *MNRAS*, 422, 2465  
 Käpylä, P. J., Mantere, M. J., & Brandenburg, A. 2012b, *ApJ*, 755, L22  
 Kemel, K., Brandenburg, A., Kleeorin, N., & Rogachevskii, I. 2012, *Astron. Nachr.*, 333, 95  
 Kleeorin, N., Mond, M., & Rogachevskii, I. 1996, *A&A*, 307, 293  
 Kleeorin, N., & Rogachevskii, I. 1994, *Phys. Rev. E*, 50, 2716  
 Kleeorin, N.I., Rogachevskii, I.V., & Ruzmaikin, A.A. 1989, *Sov. Astron. Lett.*, 15, 274  
 Kleeorin, N. I., Rogachevskii, I. V., Ruzmaikin, A. A. 1990, *Sov. Phys. JETP*, 70, 878  
 Kochukhov, O., Mantere, M. J., Hackman, T., & Ilyin, I. 2013, *A&A*, 550, A84  
 Losada, I. R., Brandenburg, A., Kleeorin, N., & Rogachevskii, I. 2014, *A&A*, 564, A2  
 Mitra, D., Tavakol, R., Käpylä, P. J., & Brandenburg, A. 2010, *ApJ*, 719, L1  
 Mitra, D., Brandenburg, A., Kleeorin, N., Rogachevskii, I. 2014, *MNRAS*, 445, 761  
 Nelson, N. J., & Miesch, M. S. 2014, *Plasm. Phys. Control. Fusion*, 56, 064004  
 Parker, E. N. 1955, *ApJ*, 121, 491  
 Parker, E. N. 1979, *ApJ*, 232, 291  
 Rempel, M., & Cheung, M. C. M. 2014, *ApJ*, 785, 90  
 Rogachevskii, I., & Kleeorin, N. 2007, *Phys. Rev. E*, 76, 056307  
 Saar, S. H., & Linsky, J. L. 1985, *ApJ*, 299, L47  
 Shukurov, A., Sokoloff, D., & Ruzmaikin, A., 1985, *Magnetohydrodynamics*, 1, 9  
 Stefani F., & Gerbeth G., 2005, *Phys. Rev. Lett*, 94, 184506  
 Stein, R. F., & Nordlund, Å. 2012, *ApJ*, 753, L13  
 Warnecke, J., Losada, I. R., Brandenburg, A., Kleeorin, N., & Rogachevskii, I. 2013, *ApJ*, 777, L37  
 Yadav, R. K., Gastine, T., Christensen, U. R., & Reiners, A., 2014, *arXiv:1407.3187*